Hybrid Proca-boson stars

Tian-Xiang Ma, Chen Liang, Jie Yang,* and Yong-Qiang Wang†

Key Laboratory of Quantum Theory and Applications of MoE, Lanzhou Center for Theoretical Physics, Lanzhou University, Lanzhou 730000, China;
Key Laboratory of Theoretical Physics of Gansu Province, Institute of Theoretical Physics and Research Center of Gravitation, Lanzhou University, Lanzhou 730000, China;
and School of Physical Science and Technology, Lanzhou University, Lanzhou 730000, China

(Received 31 May 2023; accepted 13 September 2023; published 6 November 2023)

In this paper, we construct a hybrid boson star model composed of a complex scalar field and a Proca field. The scalar field and the Proca field are both in their ground state. The model is numerically solved to obtain families of solutions for different mixed states, considering both synchronized and nonsynchronized cases. By examining the relation between the ADM mass and the synchronized frequency $\tilde{\omega}$ or the nonsynchronized frequency $\tilde{\omega}_P$, we identify several types of solution families for the hybrid Proca-boson stars. In addition to solutions that intersect with the scalar field and the Proca field at each end, there are also several types of *multibranch* mixed-state solutions. The characteristics of various solutions are analyzed and discussed in detail. We calculate the binding energy E of the hybrid Proca-boson stars and provide the relationship between E and both the synchronized frequency $\tilde{\omega}$ and the nonsynchronized frequency $\tilde{\omega}_P$. Furthermore, we obtain the stability of the corresponding hybrid star solution families from the above analyses.

DOI: 10.1103/PhysRevD.108.104011

I. INTRODUCTION

The latest cosmological data suggest that about 26% of cosmic content is dark matter (DM) [1]. However, the basic nature of DM is ambiguous. Among the many assumptions, there are several different views—some believe that DM consists of weakly interacting massive particles [2], while others propose that the mass of these dark matter particles is contributed by primordial black holes [3]. In addition to these two models, there is a novel idea that boson stars could also be a candidate for dark matter [4–6], namely macroscopic Bose-Einstein condensates formed by superlight bosons/fields under gravity. The gravitational structure and mass distribution of different scalar dark matter in the Universe can be explained by changing the mass of the scalar field or introducing the self-interaction term [7,8] to change some properties of the boson star. The boson star model has become one of the important candidates for dark matter, since it plays an important role in studying the dynamics of early star clusters [9], the rotation curves of low-surface-brightness galaxies [10], the dynamics of the Galactic Center [11–13], and the formation of supermassive black holes [14].

The study of the boson star model can be traced back to the 1960s. D. J. Kaup coupled the complex scalar field with the four-dimensional Einstein gravity [15] and then obtained the spherical symmetric solution of the Einstein-Klein-Gordon equation. In the same period, R. Ruffini and S. Bonazzola solved a model of coupling a real scalar field and gravity [16], and they obtained the same solution as well. Later, the soliton solution of the object formed by the scalar field under the gravitational interaction was called a boson star. Since then, various studies have been conducted around the boson star model. The self-interacting boson star can be obtained by adding the self-interacting term (the quartic or sextic term) to the Lagrangian density [17–20]. A charged boson star is obtained by coupling a complex scalar field with an electromagnetic field [21–25]. The Newtonian boson star is obtained by solving the Einstein-Klein-Gordon equation in the Newtonian limit [26,27]. In addition, others have studied rotating boson stars with angular momentum [28–31]. Gravity can also be coupled to a field with a nonzero spin [32–36]. In 2015, Brito *et al.* studied the static solution of a system with a Proca field (spin 1) coupled to gravity, called a Proca star [32]. Soon after, I. Salazarlandea and F. Garciaka constructed models of charged Proca stars [24]. In addition to coupling to the boson fields, Finster *et al.* [33] also constructed a spherically symmetric Dirac star coupled by two spin-1/2 spinor fields and Einstein's gravity. References [34–36] consider a system coupled by an axion field and a complex scalar field, called an axion boson star (ABS). Their work greatly enriched the boson star model and allowed the development of this research

*Corresponding author: yangjiev@lzu.edu.cn
†Corresponding author: yqwang@lzu.edu.cn

 © 2023 American Physical Society

field to flourish. In recent years, with the development of astrophysics, boson stars are also considered to be one of the candidates for dark matter; besides, they have been widely used in black hole shadow simulation [37–39] and analysis of gravitational wave signals [40–43].

Other recent studies have shown systems in which gravity is coupled to multiple matter fields, called multistate boson stars. In Ref. [44], Bernal *et al.* constructed a system consisting of two complex scalar fields—the ground state and the first excited state. Later, Refs. [17,28] studied the rotating multistate boson stars. The matter field of spherically symmetric boson stars can also be extended to an odd number of complex scalar fields [45,46].

Some recent work has shown that the Proca star plays an important role in the simulation of black hole shadows [37,47,48] and gravitational wave signal analysis [43], etc. Multifield models including the Proca field were also studied in Ref. [49]. The multifield boson star models studied by previous people are mostly composed of two complex scalar fields [17]. In Ref. [50], a spherically symmetric boson star solution coupled by a complex scalar field and two Fermi fields (spin $1/2$) is also studied. The main focus of this paper is to study the mixed-state solutions minimally coupled by two boson fields with different spins (spin 0 and 1). The aim of this work is to solve the Einstein-Proca-Klein-Gordon equation numerically, construct a spherically symmetric boson star composed of a Proca field and a complex scalar field, and study the properties of its solutions.

This paper is organized as follows: In Sec. II, we propose a four-dimensional Einstein gravity model minimally coupled with a complex scalar field and a Proca field. In Sec. III, the boundary conditions of Proca-boson stars are studied. In Sec. IV, we show the numerical results obtained by solving the model, and we show the properties of the mixed-state solutions in two different cases. In Sec. V, we summarize and describe possible future work.

II. THE MODEL SETUP

We consider the minimal coupling of a Proca field and a complex scalar field to $(3+1)$-dimensional Einstein gravity. The action is given by

$$S=\int\sqrt{-g}d^4x\left(\frac{R}{16\pi G_0}+\mathcal{L}_S+\mathcal{L}_P\right), \tag{1}$$

where G_0 is the gravitational constant, R is the Ricci scalar, $\mathcal{L}_S$ and $\mathcal{L}_P$ represent the Lagrangians of the scalar field and the Proca field, respectively, and their specific forms are

$$\begin{aligned}\mathcal{L}_S&=-g^{\alpha\beta}\bar{\Phi}_{,\alpha}\Phi_{,\beta}-\mu_S^2\bar{\Phi}\Phi,\\ \mathcal{L}_P&=-\frac{1}{4}\mathcal{F}_{\alpha\beta}\bar{\mathcal{F}}^{\alpha\beta}-\frac{1}{2}\mu_P^2\mathcal{A}_\alpha\bar{\mathcal{A}}^\alpha,\end{aligned} \tag{2}$$

where Φ and $\mathcal{A}$ are functions of complex scalar and Proca fields, respectively; $\bar{\Phi}$ and $\bar{\mathcal{A}}$ are complex conjugates of their corresponding fields; and $\mathcal{F}=d\mathcal{A}$.

The corresponding energy-momentum tensor can be obtained from the Lagrangian, where $T^S_{\alpha\beta}$ and $T^P_{\alpha\beta}$ represent the energy-momentum tensor of the scalar field and Proca field, respectively:

$$\begin{aligned}T^S_{\alpha\beta}=&\bar{\Phi}_{,\alpha}\Phi_{,\beta}+\bar{\Phi}_{,\beta}\Phi_{,\alpha}\\&-g_{\alpha\beta}\left[\frac{1}{2}g^{\gamma\delta}(\bar{\Phi}_{,\gamma}\Phi_{,\delta}+\bar{\Phi}_{,\delta}\Phi_{,\gamma})+\mu_S^2\bar{\Phi}\Phi\right],\end{aligned} \tag{3}$$

$$\begin{aligned}T^P_{\alpha\beta}=&\frac{1}{2}(\mathcal{F}_{\alpha\sigma}\bar{\mathcal{F}}_{\beta\gamma}+\bar{\mathcal{F}}_{\alpha\sigma}\mathcal{F}_{\beta\gamma})g^{\sigma\gamma}-\frac{1}{4}g_{\alpha\beta}\mathcal{F}_{\sigma\tau}\bar{\mathcal{F}}^{\sigma\tau}\\&+\frac{1}{2}\mu_P^2[\mathcal{A}_\alpha\bar{\mathcal{A}}_\beta+\bar{\mathcal{A}}_\alpha\mathcal{A}_\beta-g_{\alpha\beta}\mathcal{A}_\sigma\bar{\mathcal{A}}^\sigma].\end{aligned} \tag{4}$$

The field equation is obtained by the variation of the Lagrange:

$$R_{\alpha\beta}-\frac{1}{2}g_{\alpha\beta}R=8\pi G_0(T^S_{\alpha\beta}+T^P_{\alpha\beta}), \tag{5}$$

$$\nabla^2\Phi-\mu_S^2\Phi=0, \tag{6}$$

$$\nabla_\alpha\mathcal{F}^{\alpha\beta}-\mu_P^2\mathcal{A}^\beta=0. \tag{7}$$

The action of the matter fields is invariant under the $U(1)$ transformation $\Phi\to e^{i\alpha}\Phi$, $\mathcal{A}^\beta\to e^{i\alpha}\mathcal{A}^\beta$ with a constant α. According to Noether's theorem, there are conserved currents corresponding to these two matter fields:

$$J^\alpha_S=-i(\Phi^*\partial^\alpha\Phi-\Phi\partial^\alpha\Phi^*),\quad J^\alpha_P=\frac{i}{2}[\bar{\mathcal{F}}^{\alpha\beta}\mathcal{A}_\beta-\mathcal{F}^{\alpha\beta}\bar{\mathcal{A}}_\beta]. \tag{8}$$

We can integrate the timelike component of these conserved currents on a spacelike hypersurface Σ, and there obtain the Noether charges:

$$Q_S=\int_\Sigma J^t_S, Q_P=\int_\Sigma J^t_P. \tag{9}$$

According to the static spherical symmetric Schwarzschild solution, the specific form of the ansatz of the Proca-boson star to be solved can be expressed as [51]

$$ds^2=-N(r)\sigma^2(r)dt^2+\frac{dr^2}{N(r)}+r^2(d\theta^2+\sin^2\theta d\phi^2), \tag{10}$$

where $N(r)=1-2m(r)/r$, and functions $m(r)$ and $\sigma(r)$ only depend on the radial variable r. If $\sigma^2=1$, this metric degenerates to the static spherically symmetric Schwarzschild metric:

$$ds^2 = -\left(1 - \frac{2m(r)}{r}\right)dt^2 + \frac{dr^2}{1 - \frac{2m(r)}{r}} + r^2(d\theta^2 + \sin^2\theta d\phi^2). \tag{11}$$

In addition, for the static spherically symmetric system, we use the following ansatz of the scalar and Proca fields [32]:

$$\Phi = \phi(r)e^{-i\omega_S t}, \tag{12}$$

$$\mathcal{A} = [F(r)dt + iG(r)dr]e^{-i\omega_P t}, \tag{13}$$

where $\phi(r)$, $F(r)$, and $G(r)$ are real functions. Besides this, the constants ω_S and ω_P are the frequencies of the scalar and Proca fields, respectively. When ω_S and ω_P meet, $\omega_S = \omega_P = \omega$, we call ω the synchronized frequency. When $\omega_S \neq \omega_P$, these two frequencies are called non-synchronized frequencies.

Substituting the above ansatz into the field equations (5)–(7), we can get the following equations for $\phi(r)$, $F(r)$, $G(r)$, $m(r)$, and $\sigma(r)$:

$$\phi'' + \left(\frac{2}{r} + \frac{N'}{N} + \frac{\sigma'}{\sigma}\right)\phi' + \left(\frac{\omega_S^2}{N\sigma^2} - \mu_S^2\right)\frac{\phi}{N} = 0, \tag{14}$$

$$\frac{d}{dr}\left\{\frac{r^2[F' - \omega_P G]}{\sigma}\right\} = \frac{\mu_P^2 r^2 F}{\sigma N}, \tag{15}$$

$$\omega_P G - F' = \frac{\mu_P^2 \sigma^2 N G}{\omega_P}, \tag{16}$$

$$m' = 4\pi G_0\left[r^2 N\phi_n'^2 + \left(\mu_S^2 + \frac{\omega_S^2}{N\sigma}\right)r^2\phi^2 + \frac{r^2(F' - \omega_P G)^2}{2\sigma^2} + \frac{\mu_P^2 r^2}{2}\left(G^2 N + \frac{F^2}{N\sigma^2}\right)\right], \tag{17}$$

$$\frac{\sigma'}{\sigma} = 4\pi G_0 r\left[2\left(\phi'^2 + \frac{\omega_S^2\phi^2}{N^2\sigma^2}\right) + \mu_P^2\left(G^2 + \frac{F^2}{N^2\sigma^2}\right)\right]. \tag{18}$$

Also, the specific forms of the Noether charges obtained from Eqs. (8) and (9) are

$$Q_S = 8\pi\int_0^\infty r^2\frac{\omega_S\phi^2}{N\sigma}dr,$$
$$Q_P = 4\pi\int_0^\infty r^2\frac{(\omega_P G - F')G}{\sigma}. \tag{19}$$

III. BOUNDARY CONDITIONS

In order to solve this set of ordinary differential equations obtained in the previous section, we need to give corresponding boundary conditions for each unknown function. Since they are asymptotically flat solutions, the metric functions $m(r)$ and $\sigma(r)$ need to satisfy the boundary conditions:

$$m(0) = 0, \quad \sigma(0) = \sigma_0, \quad m(\infty) = M, \quad \sigma(\infty) = 1, \tag{20}$$

where M and σ_0 are currently unknown; the values of these two quantities can be obtained after finding the solution of the differential equation system. For the matter field functions, at infinity we require

$$\phi(\infty) = 0, \qquad F(\infty) = 0, \qquad G(\infty) = 0. \tag{21}$$

Additionally, by considering the form of the field equations (14)–(16) at the origin, we can obtain the following boundary conditions satisfied by the field functions:

$$\left.\frac{d\phi(r)}{dr}\right|_{r=0} = 0, \qquad \left.\frac{dF(r)}{dr}\right|_{r=0} = 0, \qquad G(0) = 0. \tag{22}$$

IV. NUMERICAL RESULTS

To facilitate numerical calculations, we use dimensionless quantities:

$$\tilde{r} = r/\rho, \quad \tilde{\phi} = \frac{\sqrt{4\pi}}{M_{\rm Pl}}\phi, \quad \tilde{\omega}_S = \omega_S\rho, \quad \tilde{\mu}_S = \mu_S\rho,$$
$$\tilde{F} = \frac{\sqrt{4\pi}}{M_{\rm Pl}}F, \quad \tilde{G} = \frac{\sqrt{4\pi}}{M_{\rm Pl}}G, \quad \tilde{\omega}_P = \omega_P\rho, \quad \tilde{\mu}_P = \mu_P\rho, \tag{23}$$

where $M_{\rm Pl} = 1/\sqrt{G_0}$ is the Planck mass, ρ is a positive constant whose dimension is length, and we let the constant ρ be $1/\mu_S$. Additionally, we introduce a new radial variable

$$x = \frac{\tilde{r}}{1 + \tilde{r}}, \tag{24}$$

where the radial coordinate $\tilde{r} \in [0, \infty)$, so $x \in [0, 1]$. The system of differential equations is solved numerically using the finite element method. We discretize the integration region $0 \leq x \leq 1$ into 1000 grid points, and we choose the Newton-Raphson method as our iterative approach. Finally, we set a relative error criterion of less than 10^{-5} to ensure the accuracy of the computation.

To ensure the correctness of our numerical calculations, we need to check the numerical precision by validating physical constraints [52,53], besides using the numerical analysis methods mentioned before. In this study, we compared the asymptotic mass and the Komar mass in the numerical solution, and we found that the difference between them was always less than 10^{-5}.

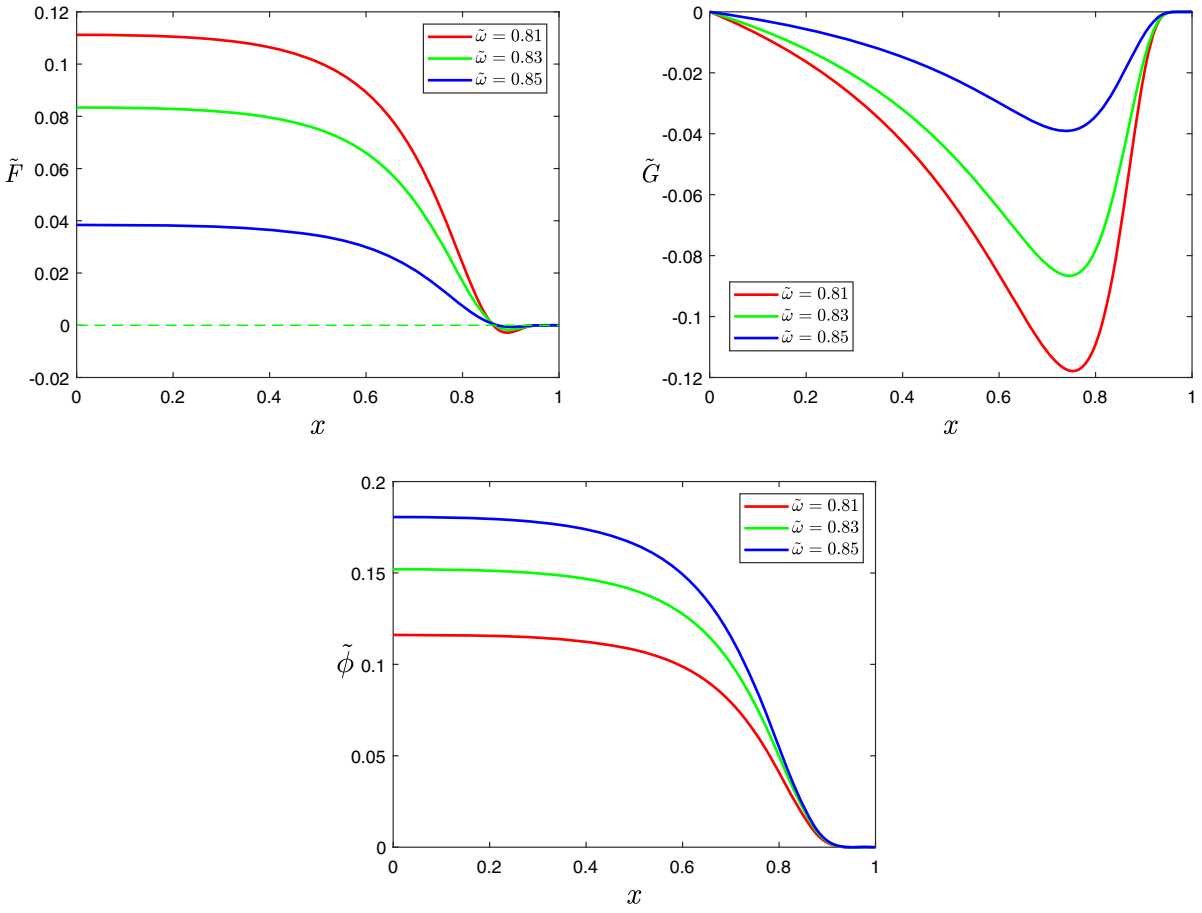

FIG. 1. Proca field functions $\tilde{F}$ and $\tilde{G}$ (top panels) and scalar field function $\tilde{\phi}$ (bottom panel) as functions of x for $\tilde{\omega} = \tilde{\omega}_S = \tilde{\omega}_P = 0.81, 0.83, 0.85$. All solutions have $\tilde{\mu}_P = 0.92$ and $\tilde{\mu}_S = 1$.

In our model, the ground-state scalar field function ϕ has no node in the radial direction, so it is represented by S_0, and the script is the total number of radial nodes of the field function. The ground-state field function F and G of the Proca field have a total of one node in the radial direction, so it is represented by P_1, and the meaning of the script is the same as that of the scalar field. So, in this model, we represent the mixed state of the scalar field and Proca field

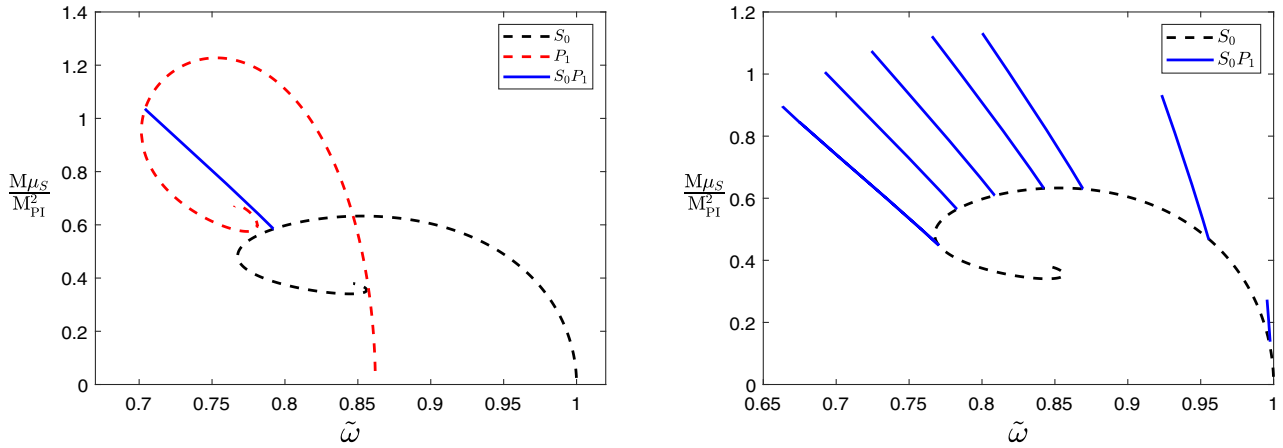

FIG. 2. Left: the ADM mass M as a function of the synchronized frequency $\tilde{\omega}$. The black dashed line represents the S_0-state solutions with $\tilde{\mu}_S = 1$, the red dashed line represents the P_1-state solutions with $\tilde{\mu}_P = 0.862$, and the blue line denotes the mixed state S_0P_1 with $\tilde{\mu}_S = 1$ and $\tilde{\mu}_P = 0.862$. Right: the ADM mass M as a function of the synchronized frequency $\tilde{\omega}$. The black dashed line represents the S_0-state solutions with $\tilde{\mu}_S = 1$. The blue lines, from left to right, represent the mixed state S_0P_1 with $\tilde{\mu}_P = 0.81$, 0.85, 0.88, 0.91, 0.93, 0.98, 0.999, and all solutions have $\tilde{\mu}_S = 1$.

in terms of S_0P_1. Next, we will analyze the different classifications of solution families of Proca-boson stars in detail.

A. Synchronized frequency

Based on the characteristics of mixed-state solutions, we categorize the synchronized frequency solution families into three types: the *one-branch* solution family, *two-branch* solution family, and *multibranch* solution family. There is a one-to-one correspondence between the mixed-state *one-branch* solution and the synchronized frequency $\tilde{\omega}$, but for the *two-branch* solution, when $\tilde{\omega}$ is valued in some ranges, one $\tilde{\omega}$ corresponds to two different solutions. Similarly, *multibranch* solutions will have one $\tilde{\omega}$ corresponding to more than two solutions. According to our numerical results, when $0.808 < \tilde{\mu}_P < 1$, the mixed-state solution is of the *one-branch* type. When $0.801 < \tilde{\mu}_P \leq 0.808$, the mixed-state solution is of the *multibranch* type. When $0.772 \leq \tilde{\mu}_P \leq 0.801$, the mixed-state solution is of the *two-branch* type. We will explore these families of solutions in detail next.

1. One-branch

The relation between the field function $\tilde{F}$, $\tilde{G}$, $\tilde{\phi}$ and the synchronized frequency $\tilde{\omega}$ is shown in Fig. 1. For scalar field functions, $|\tilde{\phi}|_{\max}$ increases as $\tilde{\omega}$ increases; For Proca field functions, $|\tilde{F}|_{\max}$ and $|\tilde{G}|_{\max}$ decrease as $\tilde{\omega}$ increases. According to the analysis of Fig. 1, the function $\tilde{F}$ has one node, while $\tilde{G}$ and $\tilde{\phi}$ have no node, which means that the mixed state is the S_0P_1 state—that is, the corresponding scalar field and Proca field are both in the ground state. Next, we will examine the properties of the S_0P_1 state in detail.

Figure 2 shows the relationship between ADM mass and synchronized frequency $\tilde{\omega}$, where we take different values of $\tilde{\mu}_P$ to obtain a *one-branch* solution for different mixed

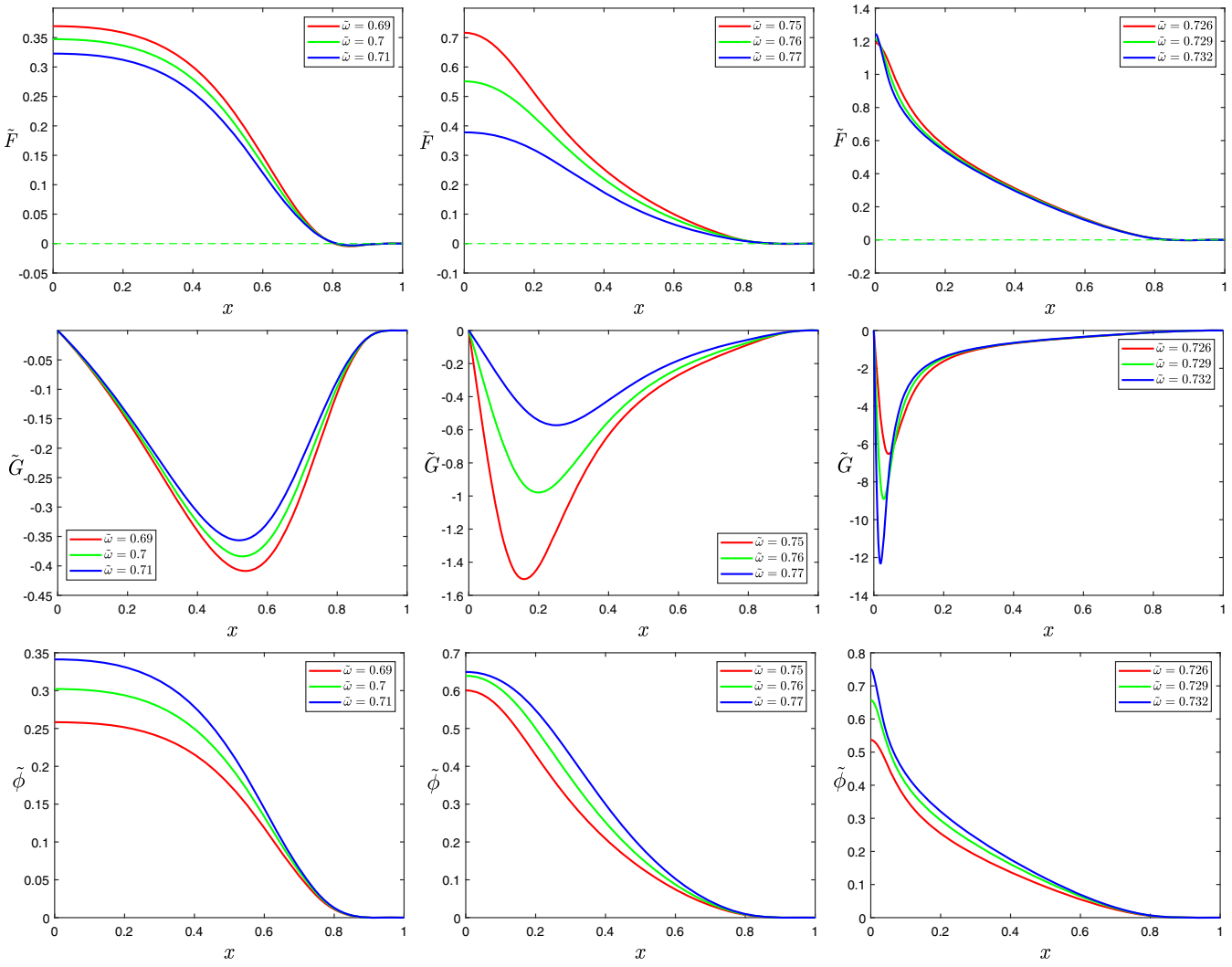

FIG. 3. Proca field functions $\tilde{F}$ (top panel) and $\tilde{G}$ (middle panel), and scalar field function $\tilde{\phi}$ (bottom panel) as functions of x with several values of synchronized frequency $\tilde{\omega}$, where the field functions on the first, second, and third branches are located in the first, second, and third rows. All solutions have $\tilde{\mu}_P = 0.808$ and $\tilde{\mu}_S = 1$.

states. The black dashed line represents the S_0-state solutions of the boson stars with $\tilde{\mu}_S = 1$, the red dashed line represents the P_1-state solutions of the Proca stars, and the blue line denotes the mixed state S_0P_1. The relationship between the ADM mass and the synchronized frequency is similar to the cases of the $^1S^2S$ or $^1S^2P$ of the Rotating multistate boson stars (RMSBSs) in Ref. [28]. It can be seen from the image that S_0P_1 has only one branch, that the ADM mass decreases with the increase of frequency, and that the two ends of the blue line fall on the black and red spiral dashed lines. As can be seen from Fig. 1, $|\tilde{\phi}|_{\max}$ decreases when the frequency decreases, and when the frequency decreases to the minimum value, the mixed-state solution falls on the Proca single field curve. At this time, the ADM mass reaches the maximum value, the amplitude of the scalar field function decreases to 0, only the Proca field remains, and the mixed star becomes a Proca star. Similarly, when the frequency increases to the maximum value, the ADM mass reaches the minimum value, and $|\tilde{F}|_{\max}$ and $|\tilde{G}|_{\max}$ decrease to 0, leaving only the scalar field remaining and transforming the mixed star into a boson star.

As can be seen from Fig. 2, when we gradually reduce $\tilde{\mu}_P$, the intersection point of the mixed state and two single-field curves will gradually move from the larger part of the synchronized frequency of the first branch to the inflection point of the first branch, and then pass the inflection point and move along the second branch to the part of the increased synchronized frequency. The synchronized frequency range of the mixed-state solution will also gradually increase until the *multibranch* solution appears.

In Table I, the existence range of the synchronized frequency $\tilde{\omega}$ and the range of M are shown for several different values of the Proca field mass $\tilde{\mu}_P$ for the *one-branch* solution family. As $\tilde{\mu}_P$ increases, the existence domain of $\tilde{\omega}$ decreases, while $M_{\max}$ and $M_{\min}$ both first increase and then decrease. The existence range of M does not change significantly when $\tilde{\mu}_P$ is small. However, when $\tilde{\mu}_P$ is large, the existence domain of M rapidly decreases with the decrease of the existence domain of $\tilde{\omega}$.

2. Multibranch

Unlike Fig. 1, in the case of *multibranch* solutions, the field functions $\tilde{F}$, $\tilde{G}$, $\tilde{\phi}$, and the synchronized frequency $\tilde{\omega}$ are no longer in a one-to-one correspondence. Their relationship is shown in Fig. 3, where the first, second, and third rows represent the first branch, second branch, and third branch of the *multibranch* solution, respectively. For the first and second branches, the field functions $|\tilde{F}|_{\max}$, $|\tilde{G}|_{\max}$, and $|\tilde{\phi}|_{\max}$ vary with the synchronized frequency $\tilde{\omega}$ in the same manner as *one-branch* solutions. For the third branch, the field functions $|\tilde{F}|_{\max}$, $|\tilde{G}|_{\max}$, and $|\tilde{\phi}|_{\max}$ increase with the increase of synchronized frequency.

The relationship between the ADM mass and the synchronized frequency can be observed from Fig. 4. In Fig. 2, when $\tilde{\mu}_P = 0.81$, the mixed-state solution is almost tangent to the second branch of the scalar field curve. If we continue to reduce the value of $\tilde{\mu}_P$, the right end of the mixed-state solution will not fall on the scalar field curve, but will instead appear as a spiral. In this type of solution family, the left end of the first branch of the mixed state is similar to the *one-branch* case, still starting from the Proca field helix. However, for the mixed state, there are still some differences. After passing the inflection point of the first branch, the second branch is extended, and then the next inflection point is passed again, and the third branch is extended, finally forming a helix. There is no disappearance of either the Proca field or scalar field in the mixed state. In short, the *multibranch* solution family is both

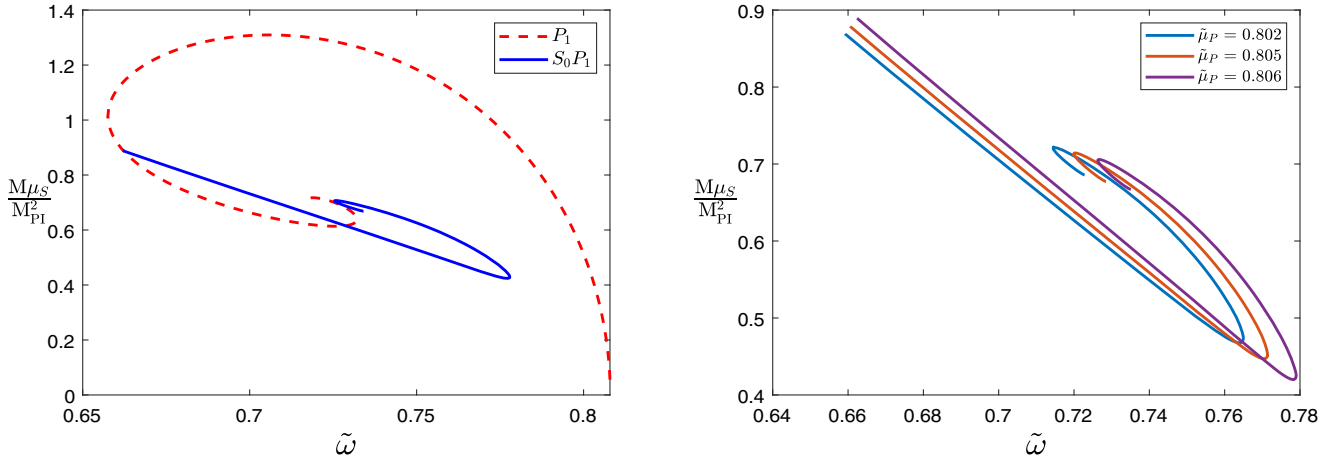

FIG. 4. Left: the ADM mass M as a function of the synchronized frequency $\tilde{\omega}$. The black dashed line represents the S_0-state solutions with $\tilde{\mu}_S = 1$, the red dashed line represents the P_1-state solutions with $\tilde{\mu}_P = 0.808$, and the blue line denotes the mixed state S_0P_1 with $\tilde{\mu}_S = 1$ and $\tilde{\mu}_P = 0.808$. Right: the ADM mass M as a function of the synchronized frequency $\tilde{\omega}$. The light blue, red, and purple lines denote the mixed state S_0P_1, with $\tilde{\mu}_P = 0.802$, 0.805, and 0.806, respectively. The black dashed line represents the S_0-state solutions with $\tilde{\mu}_S = 1$. All solutions have $\tilde{\mu}_S = 1$.

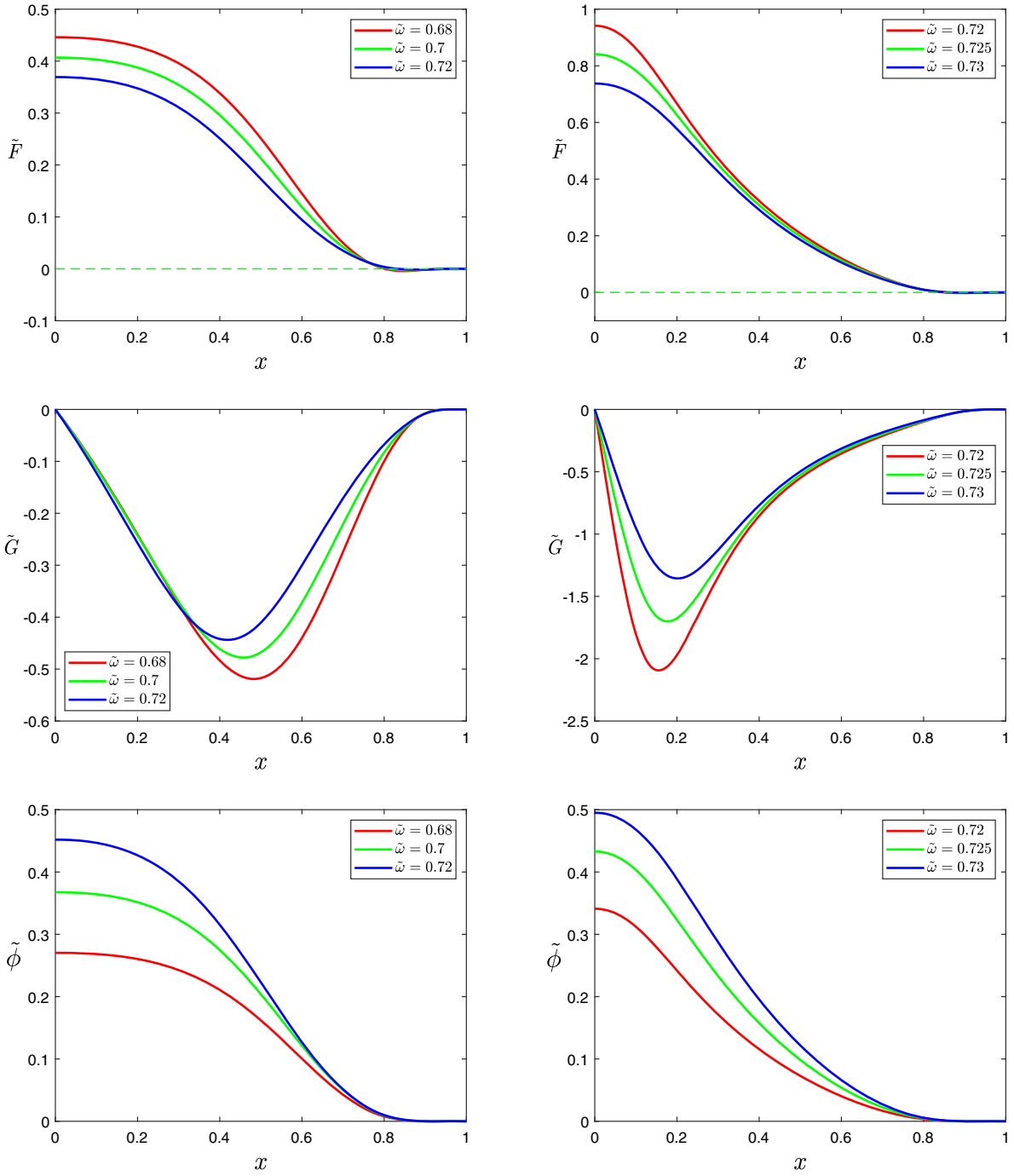

FIG. 5. Proca field functions $\tilde{F}$ (top panel) and $\tilde{G}$ (middle panel), and the scalar field function $\tilde{\phi}$ (bottom panel) as functions of x with several values of synchronized frequency $\tilde{\omega}$, where the field functions on the first and second branches are located in the first and second columns. All solutions have $\tilde{\mu}_P = 0.79$ and $\tilde{\mu}_S = 1$.

different from the *one-branch* solution family and more complex than the *one-branch* solution family.

In Table II, the domain of existence for the synchronized frequency $\tilde{\omega}$ is presented, with varying values of $\tilde{\mu}_P$, as well as the range of values for M in the *multibranch* solution family. As $\tilde{\mu}_P$ increases, the domain of existence for both the first and second branches gradually expands, while that of the third branch remains relatively unchanged. $M_{\max}$ exhibits a gradual upward trend, while $M_{\min}$ displays a gradual downward trend. The range of values for M expands as the domain of existence for $\tilde{\omega}$ increases.

3. Two-branch

In Fig. 5, the graph of the field functions $\tilde{F}$, $\tilde{G}$, $\tilde{\phi}$ is different from the previous two cases. The first and second

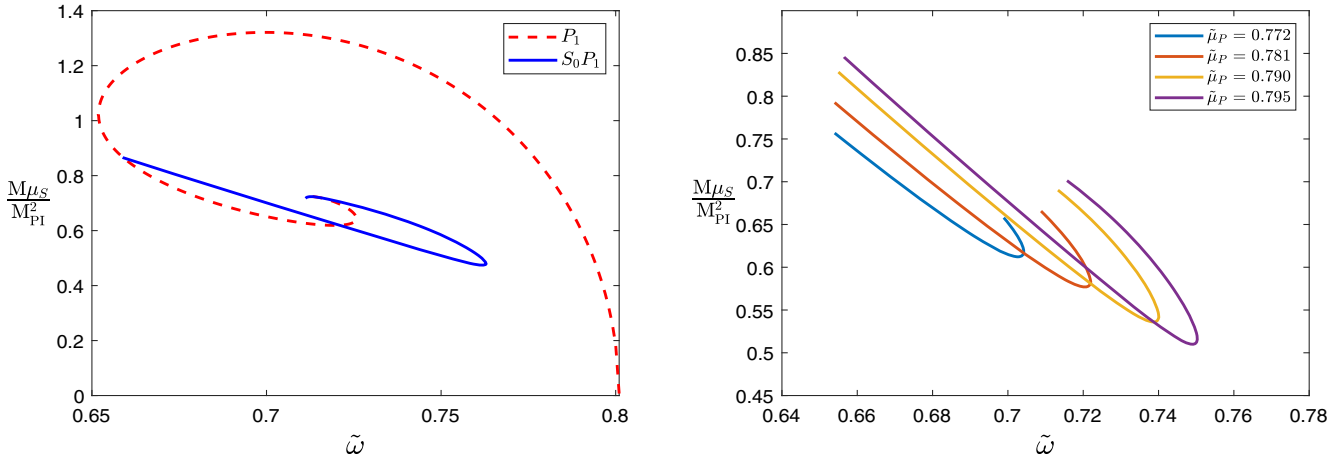

FIG. 6. Left: the ADM mass M as a function of the synchronized frequency $\tilde{\omega}$. The red dashed line represents the P_1-state solutions with $\tilde{\mu}_P = 0.801$, and the blue line denotes the mixed state S_0P_1 with $\tilde{\mu}_S = 1$ and $\tilde{\mu}_P = 0.801$. Right: the ADM mass M as a function of the synchronized frequency $\tilde{\omega}$. The light blue, red, orange, and purple lines denote the mixed state S_0P_1, with $\tilde{\mu}_P = 0.772$, 0.781, 0.79, and 0.795, respectively. The black dashed line represents the S_0-state solutions with $\tilde{\mu}_S = 1$. All solutions have $\tilde{\mu}_S = 1$.

columns of graphs represent the first and second *two-branch* solutions, respectively. The *two-branch* solution is similar to the *one-branch* solution, with $|\tilde{F}|_{\max}$ and $|\tilde{G}|_{\max}$ decreasing as $\tilde{\omega}$ increases, while $|\tilde{\phi}|_{\max}$ increases with an increase in the synchronized frequency $\tilde{\omega}$. For the second branch, the field functions $|\tilde{F}|_{\max}$, $|\tilde{G}|_{\max}$, and $|\tilde{\phi}|_{\max}$ exhibit the same trend as the first branch. This is because, in the *two-branch* solution case, the mixed-state solutions should

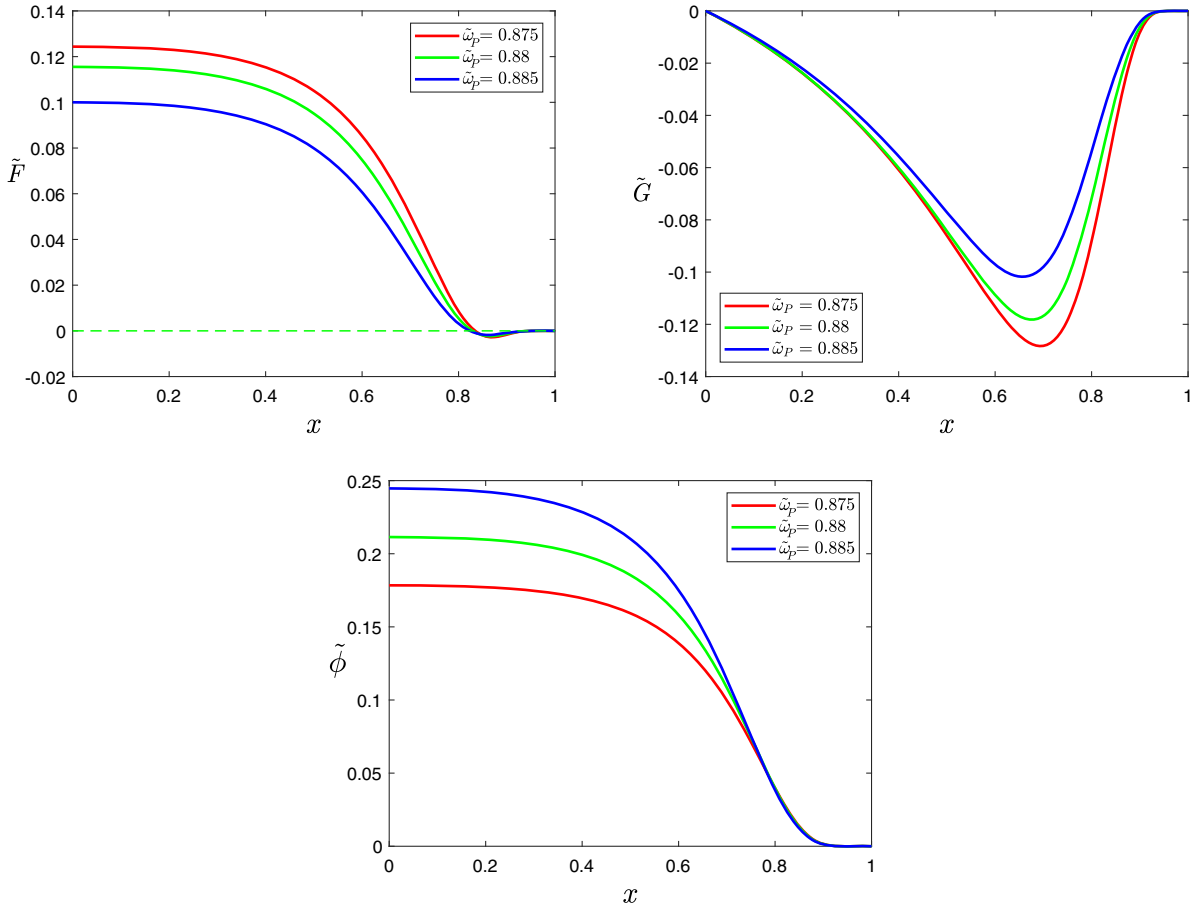

FIG. 7. Proca field functions $\tilde{F}$ and $\tilde{G}$ (top panel) and scalar field functions $\tilde{\phi}$ (bottom panel) as functions of x with $\tilde{\omega}_P = 0.875$, 0.88, 0.885. All solutions have $\tilde{\omega}_S = 0.8$ and $\tilde{\mu}_S = \tilde{\mu}_P = 1$.

degenerate into Proca field solutions when $\tilde{\omega}$ takes extreme values, so the value of $\tilde{\phi}$ is required to be 0 at this point.

In Fig. 6, we demonstrate the relationship between ADM mass and synchronized frequency $\tilde{\omega}$, similar to Fig. 2. Unlike *one-branch* solutions, mixed-state solutions are *two-branch* solutions when $\tilde{\mu}_P$ is small. This solution differs from the *one-branch* solution, where both ends fall on two single-field helices. When the synchronized frequency increases to a certain value, there exists a synchronized frequency corresponding to two distinct solutions, and the scalar field function $\tilde{\phi}$ never vanishes. The mixed-state curve still originates from the Proca field, but the right end point does not fall on the scalar field single-field curve; instead, an inflection point appears. After crossing the inflection point, as the synchronized frequency decreases, the mixed-state solution progresses along the second branch. When the final synchronized frequency reaches its minimum, the mixed-state curve intersects with the Proca single-field spiral again. At this point, the mixed state will only have a Proca field, and the mixed star will transform into a Proca star.

In Table III, the existence domain of the synchronized frequency $\tilde{\omega}$ and the values for M are shown, when the *two-branch* solution family assumes several different values of the Proca field mass $\tilde{\mu}_P$. As $\tilde{\mu}_P$ decreases, the domains of existence for both the first and second branches become narrower. When $\tilde{\mu}_P = 0.772$, the second branch is extremely narrow and nearly vanishes. $M_{\max}$ exhibits a gradually decreasing trend, while $M_{\min}$ displays a gradually increasing trend, resulting in a decrease in the range of values for M.

B. Nonsynchronized frequency

Similar to the case of synchronized frequency, we divide the mixed-state solutions in the case of nonsynchronized

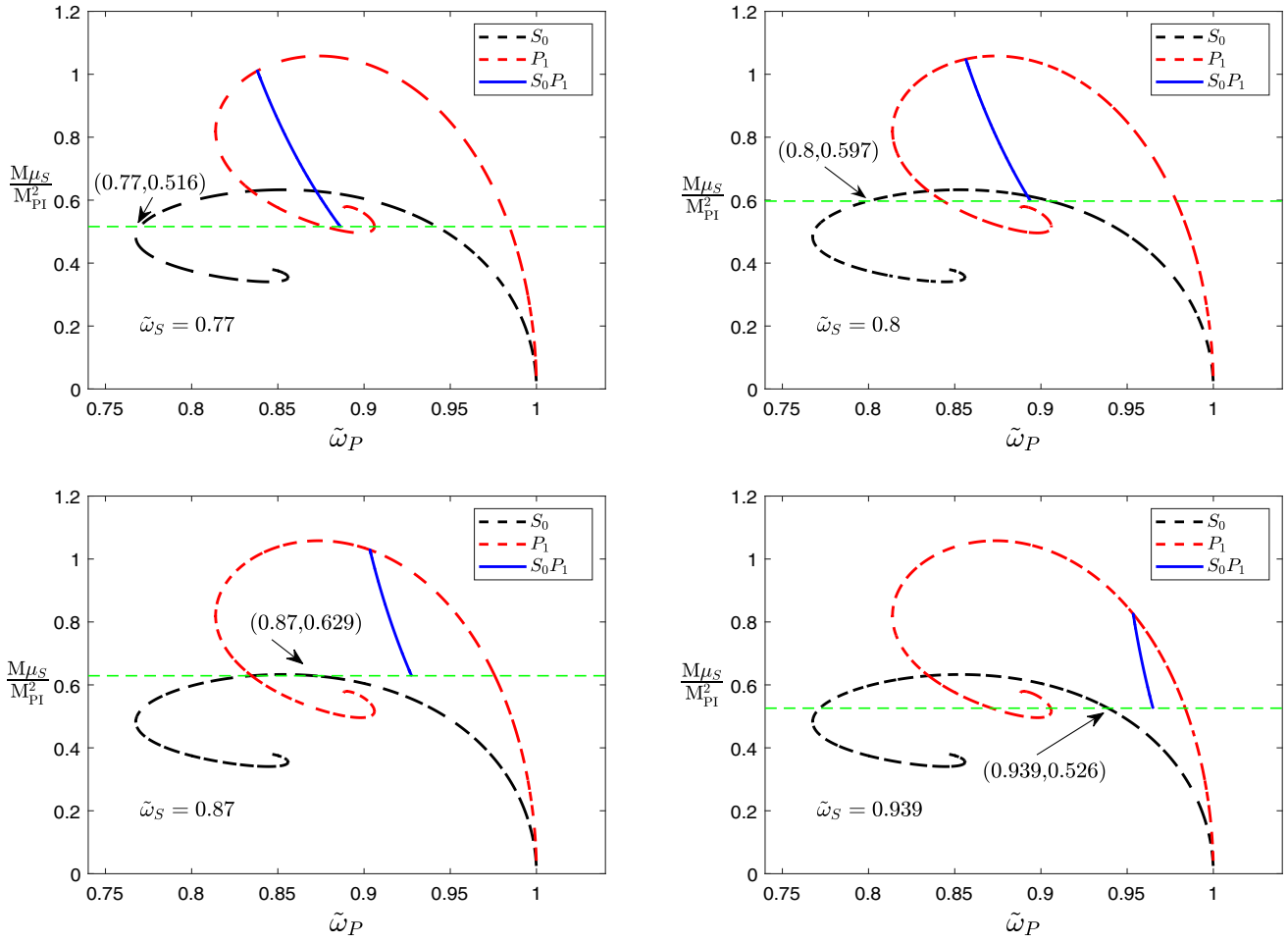

FIG. 8. The ADM mass M of the Proca-boson stars as a function of the nonsynchronized frequency $\tilde{\omega}_P$ for $\tilde{\omega}_S = 0.77$, 0.8, 0.87, 0.939. We have included the single-field curve of the scalar field in the figure (represented by a black dashed line). The value corresponding to the green horizontal dashed line in each panel is the ADM mass value of the scalar boson star solution when $\tilde{\omega}_S = 0.77$, 0.8, 0.87, 0.939, respectively, and it is also the ADM mass value of the mixed-state solution when the nonsynchronized frequency $\tilde{\omega}_P$ takes the maximum value. This indicates that when $\tilde{\omega}_P$ is at its maximum, the mixed boson star degenerates into a pure scalar boson star. The red dashed line represents the P_1-state solutions, and the blue line denotes the mixed state S_0P_1. All solutions have $\tilde{\mu}_S = \tilde{\mu}_P = 1$.

frequencies into three categories: the *one-branch-A* solution family, the *multibranch* solution family, and the *one-branch-B* solution family. When $0.768 < \tilde{\mu}_P \leq 0.939$, the mixed-state solution is part of the *one-branch-A* solution family. When $0.73 < \tilde{\mu}_P \leq 0.768$, it belongs to the mixed-state *multi-branch* solution family. When $0.7109 \leq \tilde{\mu}_P \leq 0.73$, the mixed-state solution is part of the *one-branch-B* solution family. However, there are some differences in details between the classification of solution families in the case of nonsynchronized frequencies and that in the case of a synchronized frequency. The three solution families here do not have the very obvious critical case in the case of the same frequency. We will discuss the properties of these three types of solutions in detail below.

1. One-branch-A

For the *one-branch-A* solution family, Fig. 7 displays the image of the field functions $\tilde{F}$, $\tilde{G}$, and $\tilde{\phi}$, analogous to the *one-branch* solution in the case of synchronized frequency.

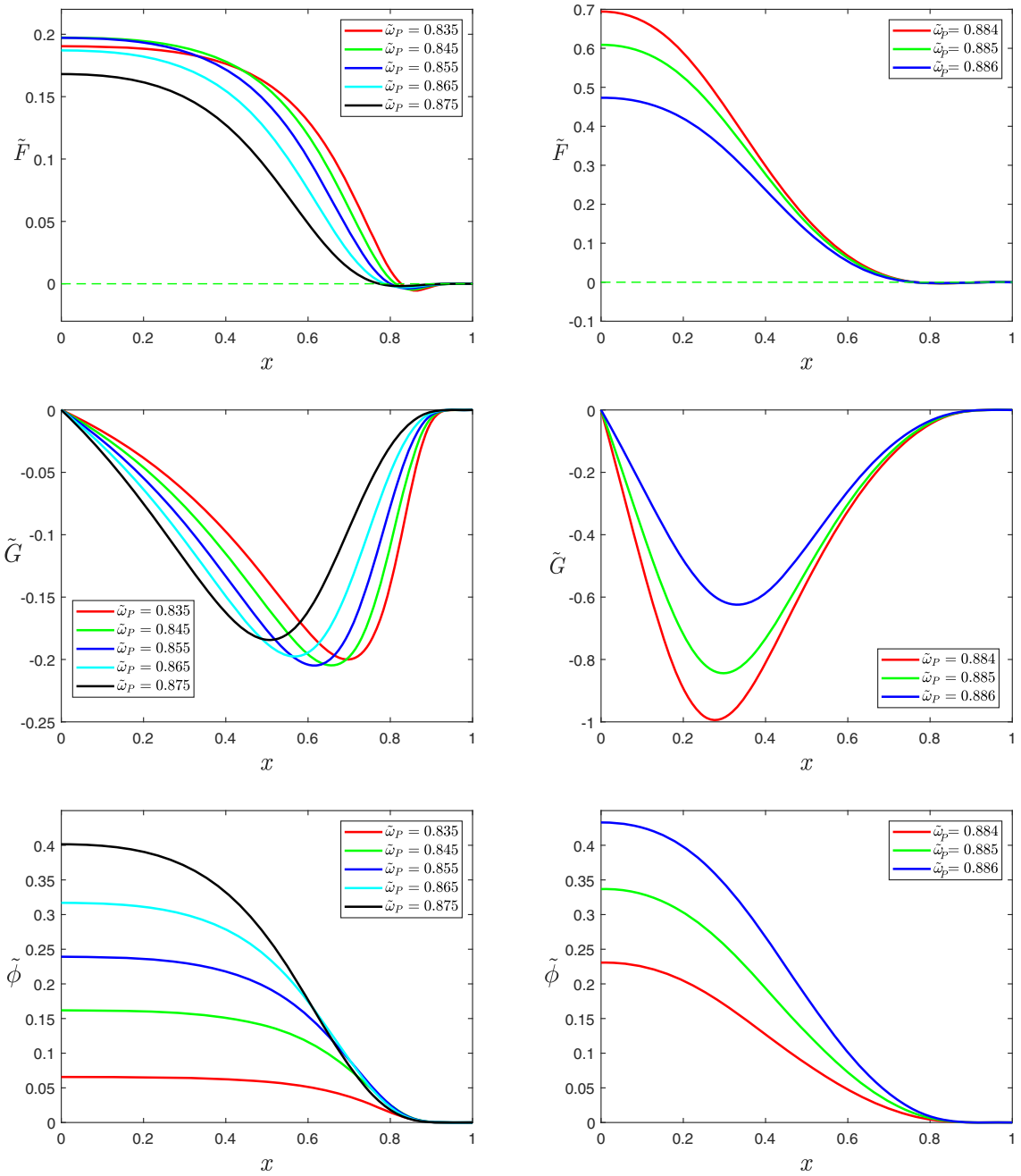

FIG. 9. Proca field functions $\tilde{F}$ (top panel) and $\tilde{G}$ (middle panel), and scalar field function $\tilde{\phi}$ (bottom panel) as functions of x with several values of synchronized frequency $\tilde{\omega}$, where the field functions on the first and second solution branches are located in the first and second rows, respectively. All solutions have $\tilde{\omega}_S = 0.76$ and $\tilde{\mu}_S = \tilde{\mu}_P = 1$.

For the scalar field function, $|\tilde{\phi}|_{\max}$ increases with an increase in the nonsynchronized frequency $\tilde{\omega}_P$. For the Proca field function, both $|\tilde{F}|_{\max}$ and $|\tilde{G}|_{\max}$ decrease as the nonsynchronized frequency $\tilde{\omega}_P$ increases.

In Fig. 8, we demonstrate the relationship between the ADM mass M and the nonsynchronized frequency $\tilde{\omega}_P$, when the scalar field frequency $\tilde{\omega}_S$ assumes different values. This solution is analogous to the *one-branch* solution in the case of synchronized frequency, where the left end of the mixed-state solution curve still falls on the single-field helix of the Proca field, and the ADM mass value at the right end is equal to the ADM mass of the single field of the scalar field when the corresponding value of $\tilde{\omega}_S$ is taken in S_0P_1. In other words, when the nonsynchronized frequency $\tilde{\omega}_P$ reaches its maximum value, the Proca field vanishes, and the mixed star transforms into a boson star. Furthermore, as $\tilde{\omega}_S$ decreases, the range of existence for the mixed-state solution gradually expands until no solution remains.

Table IV displays the domain of existence for the nonsynchronized frequency $\tilde{\omega}_P$, with varying values of the scalar field frequency $\tilde{\omega}_S$, as well as the values of $M_{\max}$ and $M_{\min}$. As $\tilde{\omega}_S$ increases, the domain of existence for $\tilde{\omega}_P$ gradually narrows, becoming quite narrow when $\tilde{\omega}_S = 0.939$. Additionally, as $\tilde{\omega}_S$ increases, both $M_{\max}$ and $M_{\min}$ first increase and then decrease.

2. Multibranch

In the case of nonsynchronized frequency, the field functions of the *multibranch* solutions are similar to those in synchronized case, as shown in Fig. 9. The first and second columns of graphs represent the first and second *two-branch* solutions, respectively. For the first branch, both $|\tilde{F}|_{\max}$ and $|\tilde{G}|_{\max}$ initially increase and then decrease with the nonsynchronized frequency $\tilde{\omega}_P$, while $|\tilde{\phi}|_{\max}$ increases as the nonsynchronized frequency $\tilde{\omega}_P$ increases. For the second branch, both $|\tilde{F}|_{\max}$ and $|\tilde{G}|_{\max}$ decrease as the nonsynchronized frequency $\tilde{\omega}_P$ increases, while $|\tilde{\phi}|_{\max}$ continues to increase with an increase in the nonsynchronized frequency $\tilde{\omega}_P$.

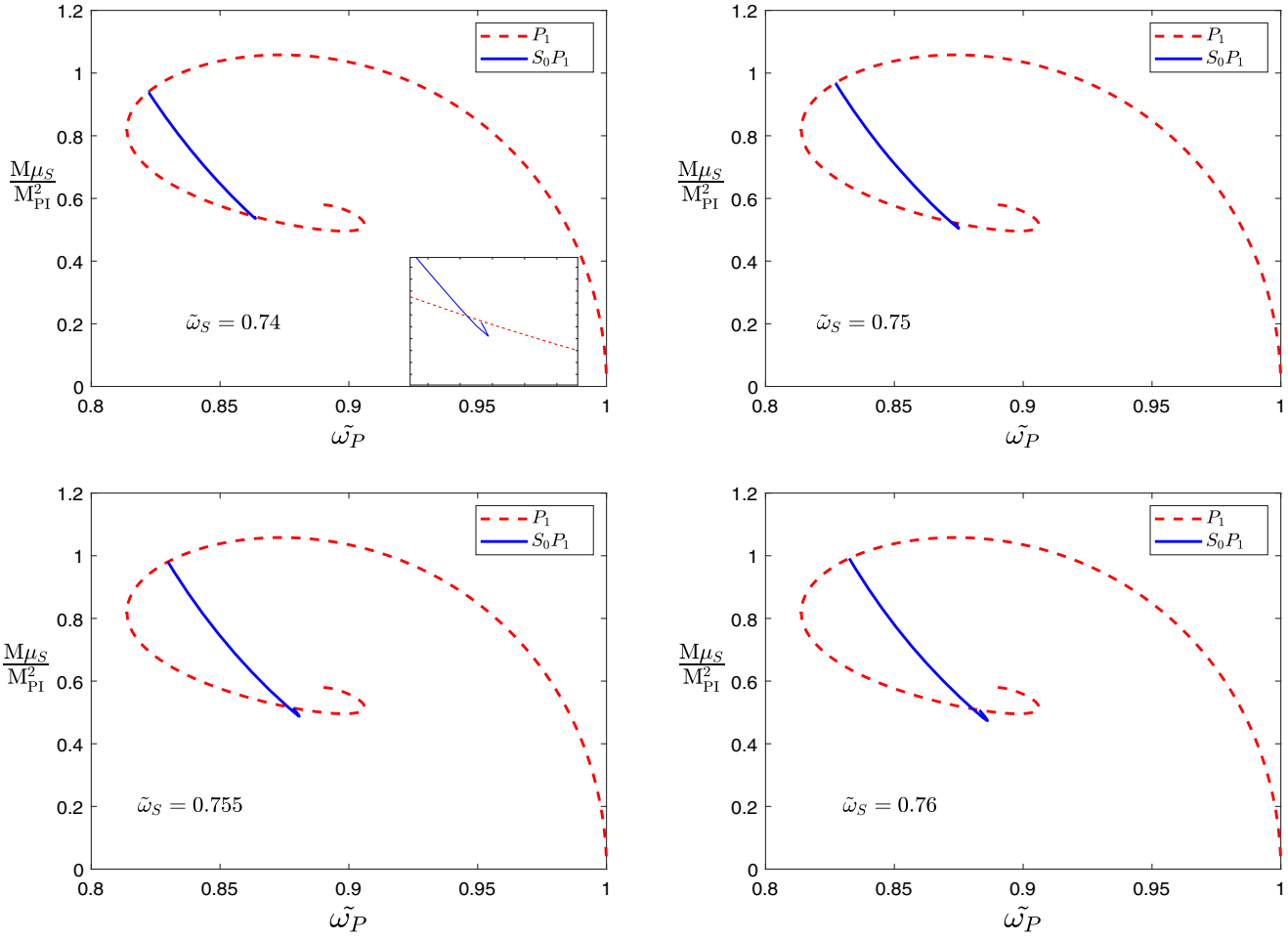

FIG. 10. The ADM mass M of the Proca-boson stars as a function of the nonsynchronized frequency $\tilde{\omega}_P$ for $\tilde{\omega}_S = 0.74, 0.75, 0.755, 0.76$. The red dashed line represents the P_1-state solutions, and the blue line denotes the mixed state S_0P_1. All solutions have $\tilde{\mu}_S = \tilde{\mu}_P = 1$.

In Fig. 10, the correlation between the mixed-state solution's ADM mass M and the nonsynchronized frequency $\tilde{\omega}_P$ is illustrated, given various values of $\tilde{\omega}_P$. It can be observed that this type of solution is similar to the *two-branch* solution in the case of synchronized frequency. The first branch also extends from the single-field curve of the Proca field and returns to form the second branch at the inflection point. The end point of the second branch intersects with the single-field curve of the Proca field again at another location. At this point, the scalar field vanishes, and the mixed star transforms into a Proca star. The difference is that, while the *two-branch* solution in the synchronized frequency case is quite smooth around the inflection point, the inflection point in the mixed-state curve in the non-synchronized frequency case is sharp. This also reflects the primary difference between the synchronized and nonsynchronized frequency cases.

In Table V, we present the domain of existence for the nonsynchronized frequency $\tilde{\omega}_P$, with varying values of the scalar field frequency $\tilde{\omega}_S$, and the values of $M_{\max}$ and $M_{\min}$. As $\tilde{\omega}_S$ decreases, the domains of existence for both the first and second branches gradually narrow. When $\tilde{\omega}_S = 0.74$, the second branch nearly vanishes, with $M_{\max}$ decreasing as $\tilde{\omega}_S$ decreases, while $M_{\min}$ increases.

3. One-branch-B

For the *one-branch-B* solution family, the amplitudes of the field functions $\tilde{F}$, $\tilde{G}$, and $\tilde{\phi}$ with the nonsynchronized frequency are shown in Fig. 11. For the scalar field function, $|\tilde{\phi}|_{\max}$ initially increases and then decreases as the nonsynchronized frequency $\tilde{\omega}_P$ increases. For the Proca field functions, both $|\tilde{F}|_{\max}$ and $|\tilde{G}|_{\max}$ increase with the nonsynchronized frequency $\tilde{\omega}_P$.

Figure 12 shows the relationship between the ADM mass M of the mixed star and the nonsynchronized frequency $\tilde{\omega}_P$, when the scalar field frequency $\tilde{\omega}_S$ assumes different values. According to Fig. 10, when $\tilde{\omega}_S = 0.74$, it remains a *two-branch* solution. If $\tilde{\omega}_S$

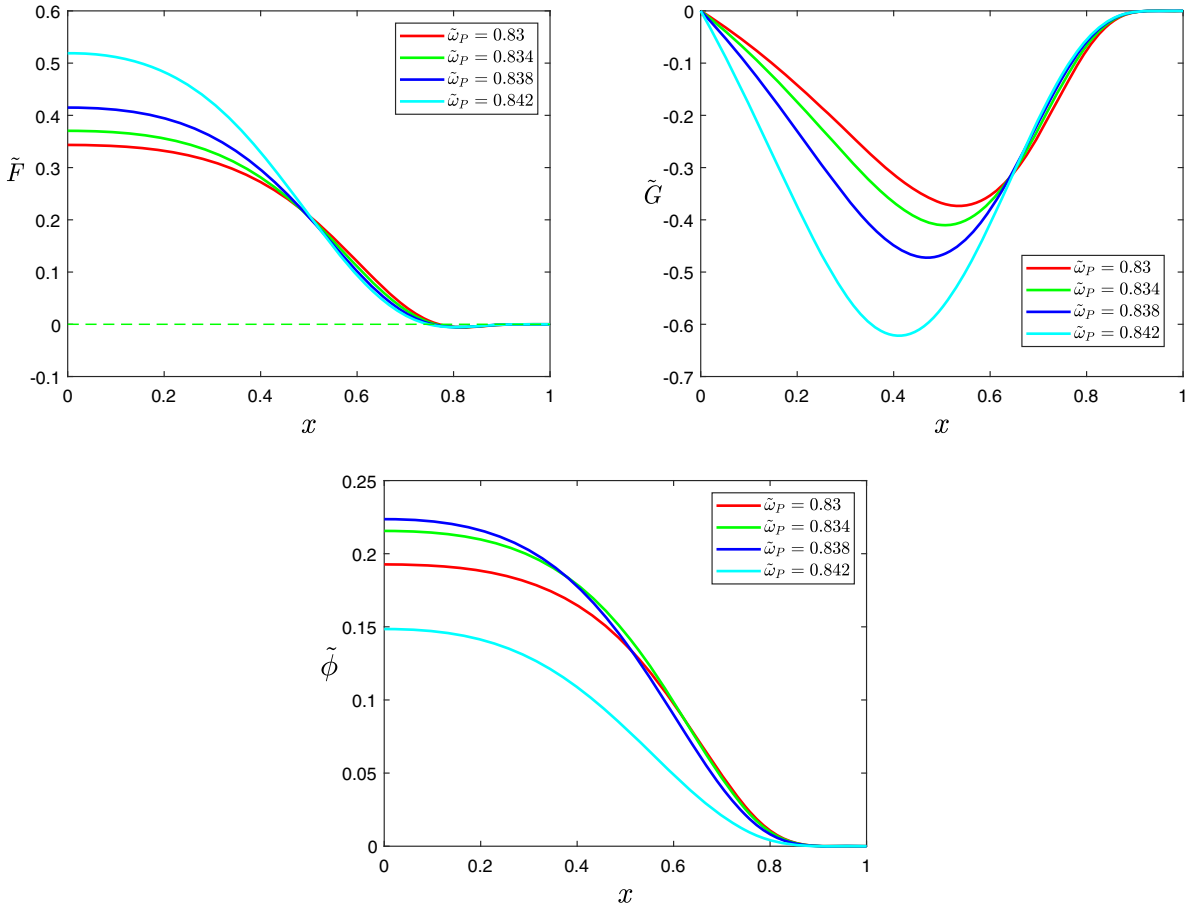

FIG. 11. Proca field functions $\tilde{F}$ (top-left panel) and $\tilde{G}$ (top-right panel) and scalar field functions $\tilde{\phi}$ (bottom panel) as functions of x with $\tilde{\omega}_P = 0.83, 0.834, 0.838, 0.842$. All solutions have $\tilde{\omega}_S = 0.722$ and $\tilde{\mu}_S = \tilde{\mu}_P = 1$.

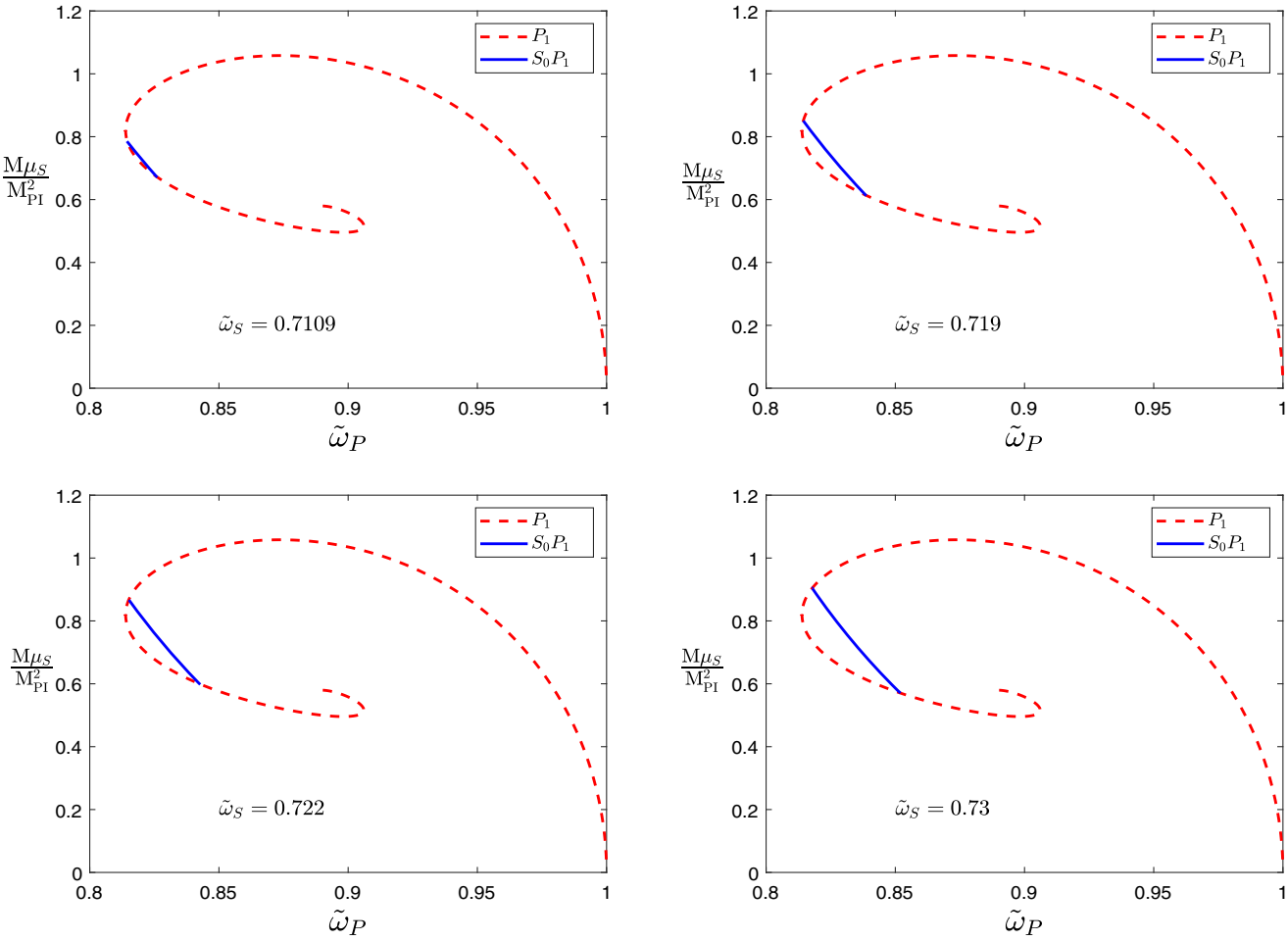

FIG. 12. The ADM mass M of the Proca-boson stars as a function of the nonsynchronized frequency $\tilde{\omega}_P$ for $\tilde{\omega}_S = 0.7109$, 0.719, 0.722, 0.73. The red dashed line represents the P_1-state solutions, and the blue line denotes the mixed state S_0P_1. All solutions have $\tilde{\mu}_S = \tilde{\mu}_P = 1$.

continues to decrease, the second branch of the *two-branch* solution will disappear, and the mixed state will transform into another *one-branch* solution. At this point, the *one-branch* solution differs from the *one-branch-A* solution family, where the two ends of the *one-branch-A* solution family intersect the Proca field curve and the scalar field curve. That is, the Proca field function must not disappear during an increase in $\tilde{\omega}_P$. For *one-branch-B* solutions, both ends of the mixed-state curve are on the Proca field curve—that is, when $\tilde{\omega}_P$ reaches its minimum or maximum, the mixed star is a Proca star. As $\tilde{\omega}_P$ increases, $|\tilde{\phi}|_{\max}$ first increases and then decreases, disappearing when $\tilde{\omega}_S$ reaches its maximum value, and the mixed star transforms into a Proca star again.

Table VI shows the range of the nonsynchronized frequency $\tilde{\omega}_P$ for different values of the scalar field frequency $\tilde{\omega}_S$, along with the $M_{\max}$ and $M_{\min}$ values. As $\tilde{\omega}_S$ decreases, the domain of existence for $\tilde{\omega}_P$ narrows, with $M_{\max}$ gradually decreasing, while $M_{\min}$ increases.

C. Binding energy

In conclusion, we examine the binding energy $E = M - \mu_S Q_S - \mu_P Q_P$ for the six solution families obtained above. Figure 13 presents the binding energy E of the mixed state versus the synchronized frequency $\tilde{\omega}$ for several values of the mass $\tilde{\mu}_P$. For the family of synchronized frequency solutions, the *one-branch* solution is unstable ($E > 0$) when $\tilde{\mu}_P$ is small. However, as $\tilde{\mu}_P$ increases, the solution gradually becomes stable within a certain frequency domain and eventually transforms into a stable ($E < 0$) mixed-state solution as $\tilde{\mu}_P$ continues to increase. The cases of *multibranch* and *two-branch* solutions exhibit identical behavior in terms of binding energy, remaining perpetually unstable.

Figure 14 presents the binding energy E of the mixed state versus the nonsynchronized frequency $\tilde{\omega}_P$ for several values of the scalar field frequency $\tilde{\omega}_S$. For the *one-branch-A* solution family, the binding energy E increases as the nonsynchronized frequency $\tilde{\omega}_P$ decreases. For the

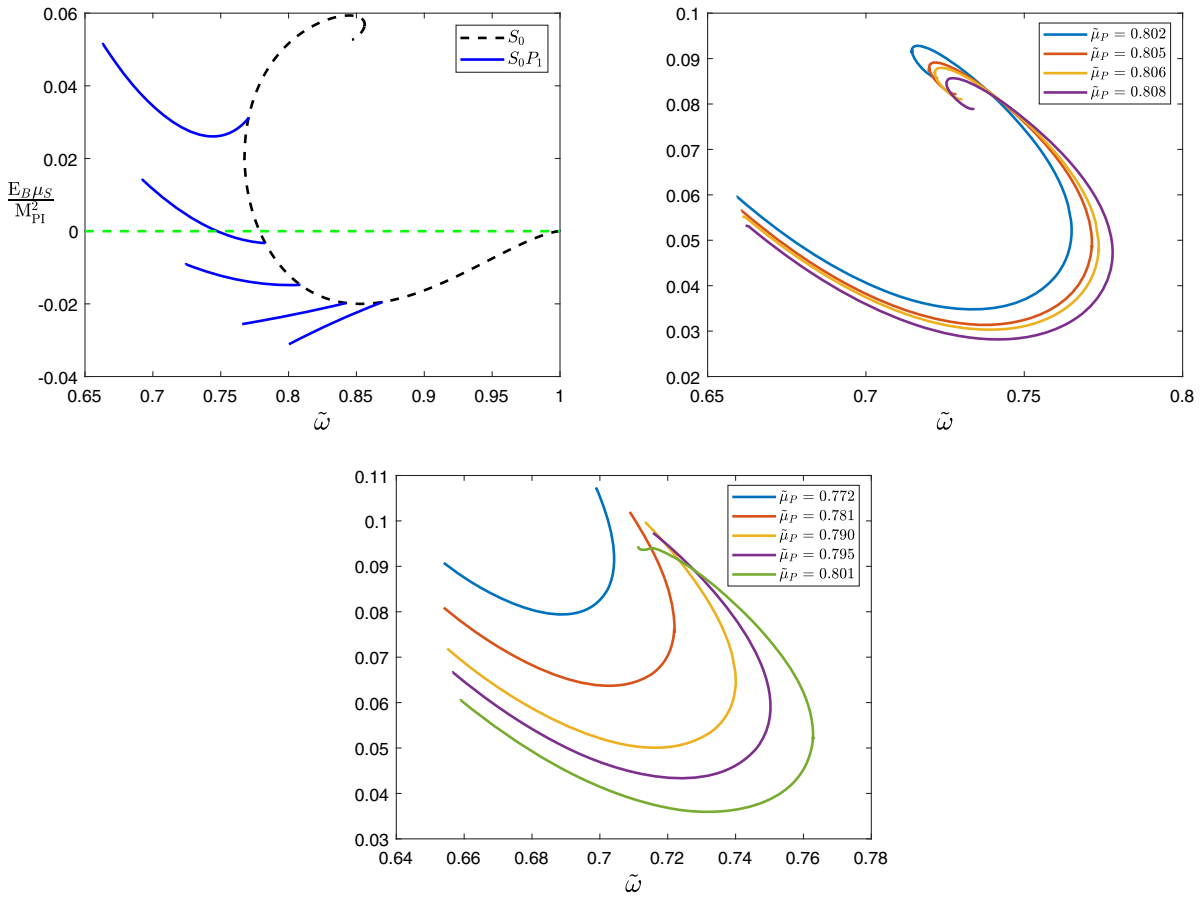

FIG. 13. Top-left: the binding energy E of the *one-branch* solution family as a function of the synchronized frequency $\tilde{\omega}$ for several values of the Proca field mass $\tilde{\mu}_P$. The black line represents the S_0-state solutions. Top-right: same as top-left panel for the *multibranch* solution family. Bottom: same as top two panels for the *two-branch* solution family. All solutions have $\tilde{\mu}_S = 1$.

multibranch and *one-branch-B* solution families, as $\tilde{\omega}_P$ increases, the binding energy E exhibits a tendency to first decrease and then increase. For the *one-branch-A* family and *multibranch* family, their solutions display stable ($E < 0$) behavior in one part of the frequency domain and unstable ($E > 0$) behavior in the remaining part, while for *one-branch-B* solutions, their solutions are perpetually unstable ($E > 0$).

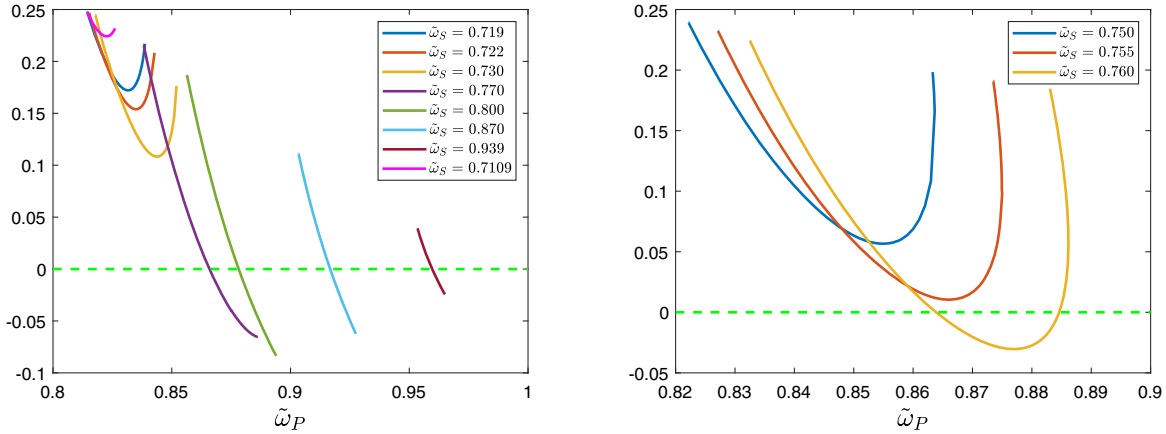

FIG. 14. Left: the binding energy E of the *one-branch* solution family as a function of the nonsynchronized frequency $\tilde{\omega}_P$ for several values of the scalar field's frequency $\tilde{\omega}_S$. Right: same as left panel for the *multibranch* solution family. All solutions have $\tilde{\mu}_S = \tilde{\mu}_P = 1$.

V. CONCLUSIONS

In this paper, we introduce a spherically symmetric hybrid Proca-boson star model consisting of a scalar field and a Proca field, both in their ground states. Additionally, we examine the characteristics of various mixed-state solutions.

For synchronized frequency solutions, we categorize mixed-state solutions into three groups based on the number of branches: *one-branch*, *two-branch*, and *multibranch* solutions. The field function of the first branch for these three solution types changes similarly. As the synchronized frequency $\tilde{\omega}$ increases, both $|\tilde{F}|_{\max}$ and $|\tilde{G}|_{\max}$ decrease, while $|\tilde{\phi}|_{\max}$ increases. In the case of *one-branch* solutions, the mass M of the mixed state decreases as the synchronized frequency $\tilde{\omega}$ increases, while the binding energy E exhibits an opposite trend. Furthermore, as we decrease the mass of the Proca field $\tilde{\mu}_P$, the existence domain of synchronized frequency solutions gradually expands. For *two-branch* solutions, the field function on the second branch changes with the synchronized frequency $\tilde{\omega}$ as well as the first branch. The image of M of the mixed state with respect to the synchronized frequency $\tilde{\omega}$ is a smooth curve. Starting from a point on the Proca single-field helix corresponding to $\tilde{\mu}_P$, the frequency reaches its maximum value at an inflection point and then decreases. The second branch appears and eventually returns to the single-field helix of the Proca field when the frequency decreases to its minimum value. The M of the first branch increases with the synchronized frequency $\tilde{\omega}$, first decreasing and then slightly increasing. The second branch is monotonically decreasing (for the critical state of $\tilde{\mu}_P = 0.801$, M slightly increases first and then monotonically decreases). For *multibranch* solutions, the image of M with respect to the synchronized frequency $\tilde{\omega}$ becomes a spiral shape. For the first and second branches, $|\tilde{F}|_{\max}$ and $|\tilde{G}|_{\max}$ decrease, and $|\tilde{\phi}|_{\max}$ increases with an increase in synchronized frequency $\tilde{\omega}$. For the third branch, however, the trend of $|\tilde{F}|_{\max}$ and $|\tilde{G}|_{\max}$ is opposite to that of the first and second branches, while $|\tilde{\phi}|_{\max}$ is consistent with that of the first and second branches. For each branch, as Proca field mass $\tilde{\mu}_P$ decreases, the existence domain of $\tilde{\omega}$ increases. Additionally, as $\tilde{\mu}_P$ decreases, $M_{\min}$ increases, while $M_{\max}$ first decreases and then increases.

In the case of nonsynchronized frequency, the mixed-state solution family is still divided into three categories: *one-branch-A* solutions, *multibranch* solutions, and *one-branch-B* solutions. *One-branch-A* is similar to the *one-branch* solution of the synchronized frequency. With an increase in the nonsynchronized frequency $\tilde{\omega}_P$, the variation of the existence domain of $|\tilde{F}|_{\max}$, $|\tilde{G}|_{\max}$, $|\tilde{\phi}|_{\max}$, mass M, and nonsynchronized frequency $\tilde{\omega}_P$ is similar to that of the *one-branch* solution family of the synchronized frequency case. However, the minimum value of M of the nonsynchronized frequency depends on $\tilde{\omega}_S$. It is equal to M of the scalar field single field of $\tilde{\mu}_S = 1$ when $\tilde{\omega}_S$ takes the same value. For *multibranch* solutions, $|\tilde{F}|_{\max}$ and $|\tilde{G}|_{\max}$ of the first branch first increase and then decrease with an increase in the nonsynchronized frequency $\tilde{\omega}_P$, while $|\tilde{\phi}|_{\max}$ is monotonically increasing. The $|\tilde{F}|_{\max}$ and $|\tilde{G}|_{\max}$ of the second branch decrease monotonically, and $|\tilde{\phi}|_{\max}$ is consistent with the trend of the first branch, still increasing monotonically. For each branch, the existence domain of the nonsynchronized frequency $\tilde{\omega}_P$ decreases as the frequency $\tilde{\omega}_S$ of the scalar field decreases. The relationship between mass M and the nonsynchronized frequency $\tilde{\omega}_P$ is similar to that between *two-branch* solutions in the synchronized frequency case but behaves differently at inflection points. It is not smooth at inflection points but appears sharply bent. Finally, when the nonsynchronized frequency $\tilde{\omega}_P$ of the second branch reaches its lowest point, the mixed-state curve falls on the Proca field. As $\tilde{\omega}_S$ decreases, both $M_{\min}$ and $M_{\max}$ decrease. For *one-branch-B* solutions, as the nonsynchronized frequency $\tilde{\omega}_P$ increases, both $|\tilde{F}|_{\max}$ and $|\tilde{G}|_{\max}$ increase, while $|\tilde{\phi}|_{\max}$ first increases and then decreases. The mass M of mixed states decreases. When the nonsynchronized frequency reaches its maximum value, the curve falls on the Proca field. The existence domain of the mixed-state nonsynchronized frequency $\tilde{\omega}_P$ increases with an increase in scalar field frequency $\tilde{\omega}_S$.

The Proca-boson star solutions presented in this paper exhibit several new solution families that differ significantly from those found in previous studies [28,50]. Through the analysis of binding energy, in the solution families of the six branches we obtained, the *multibranch* and *two-branch* solutions of the synchronized frequency case are unstable, while the other solutions are stable in some part of the frequency domain. In terms of the stability of the solution, the situation is similar to that of several solutions obtained in [44]. In future research, we plan to investigate mixed stars composed of both fields in the first excited state. Additionally, inspired by [45], we may explore the superposition of more matter fields as another possible direction for future study.

ACKNOWLEDGMENTS

This work is supported by the National Key Research and Development Program of China (Grant No. 2020YFC-2201503) and the National Natural Science Foundation of China (Grants No. 12275110 and No. 12247101). Parts of the computations were performed on the shared memory system at the Institute of Computational Physics and Complex Systems at Lanzhou University.

APPENDIX

This appendix contains Tables I–VI, where we offer a comprehensive analysis of the numerical results, including detailed data on the existence domain, ADM mass range, and binding energy of these solutions.

TABLE I. The existence domain of the synchronized frequency $\tilde{\omega}$, maximum and minimum ADM masses ($M_{\max}$ and $M_{\min}$), and maximum and minimum binding energy ($E_{\max}$ and $E_{\min}$) of the mixed state, for several values of the Proca field mass $\tilde{\mu}_P$. $\tilde{\omega}_0$ represents the value of the synchronized frequency when $E = 0$ in Fig. 2. All solutions have $\tilde{\mu}_S = 1$.

$\tilde{\mu}_P$	$\tilde{\omega}$	$M_{\max}$	$M_{\min}$	$E_{\max}$	$\tilde{\omega}_0$
0.81	0.6631–0.7704	0.894	0.448	0.051	⋯
0.85	0.6923–0.7829	1.006	0.565	0.014	0.747
0.862	0.705–0.7923	1.03	0.584	−0.009	⋯
0.88	0.7242–0.8088	1.074	0.609	−0.015	⋯
0.91	0.7657–0.8425	1.122	0.632	−0.02	⋯
0.93	0.8002–0.8694	1.132	0.63	−0.019	⋯

TABLE II. The existence domain of the synchronized frequency $\tilde{\omega}$, ADM mass (M), and binding energy (E) of the mixed state, for several values of the Proca field mass $\tilde{\mu}_P$. B_1, B_2, and B_3 represent the first, second, and third branches in Fig. 4, respectively. All solutions have $\tilde{\mu}_S = 1$.

$\tilde{\mu}_P$	B_1	B_2	B_3	E
0.802	0.659–0.765	0.715–0.765	0.715–0.723	0.035–0.093
0.805	0.661–0.771	0.72–0.771	0.72–0.729	0.031–0.089
0.806	0.661–0.774	0.722–0.774	0.722–0.730	0.03–0.088
0.808	0.662–0.778	0.725–0.778	0.725–0.734	0.028–0.086

TABLE III. The existence domain of the synchronized frequency $\tilde{\omega}$, maximum and minimum ADM masses ($M_{\max}$ and $M_{\min}$), and binding energy (E) of the mixed state, for several values of the Proca field mass $\tilde{\mu}_P$. B_1 and B_2 represent the first and second branches in Fig. 6, respectively. All solutions have $\tilde{\mu}_S = 1$.

$\tilde{\mu}_P$	B_1	B_2	$M_{\max}$	$M_{\min}$
0.772	0.654–0.7042	0.6989–0.7042	0.757	0.612
0.781	0.654–0.722	0.7088–0.722	0.793	0.577
0.79	0.655–0.74	0.7133–0.74	0.828	0.536
0.795	0.6565–0.7503	0.7157–0.7503	0.846	0.51
0.801	0.6588–0.7829	0.7112–0.7829	0.866	0.474

TABLE IV. The existence domain of the nonsynchronized frequency $\tilde{\omega}_P$, and the maximum and minimum ADM masses ($M_{\max}$ and $M_{\min}$) of the mixed state, for several values of the scalar field frequencies $\tilde{\omega}_S$. $\tilde{\omega}_0$ represents the value of the nonsynchronized frequency when $E = 0$ in Fig. 8. All solutions have $\tilde{\mu}_S = \tilde{\mu}_P = 1$.

$\tilde{\omega}_S$	$\tilde{\omega}_P$	M	E	$\tilde{\omega}_0$
0.77	0.838–0.8862	0.516–1.01	−0.066–0.216	0.866
0.8	0.844–0.8871	0.557–1.026	−0.084–0.187	0.878
0.87	0.9033–0.9275	0.629–1.029	−0.062–0.111	0.917
0.939	0.9535–0.965	0.526–0.826	−0.024–0.039	0.96

TABLE V. The existence domain of the nonsynchronized frequency $\tilde{\omega}_P$, and the maximum and minimum ADM masses ($M_{\max}$ and $M_{\min}$) of the mixed state, for several values of the scalar field frequencies $\tilde{\omega}_S$. B_1 and B_2 represent the first and second branches in Fig. 10, respectively. $\tilde{\omega}_0$ represents the value of the nonsynchronized frequency when $E = 0$ in Fig. 10. All solutions have $\tilde{\mu}_S = \tilde{\mu}_P = 1$.

$\tilde{\omega}_S$	B_1	B_2	M	$\tilde{\omega}_0$
0.74	0.8222–0.8636	0.8633–0.8636	0.538–0.934	⋯
0.75	0.8271–0.875	0.8735–0.875	0.505–0.968	⋯
0.76	0.8325–0.8861	0.883–0.8861	0.474–0.992	0.864, 0.885

TABLE VI. The existence domain of the nonsynchronized frequency $\tilde{\omega}_P$, and the maximum and minimum ADM masses ($M_{\max}$ and $M_{\min}$) of the mixed state, for several values of the scalar field frequencies $\tilde{\omega}_S$ in Fig. 12. All solutions have $\tilde{\mu}_S = \tilde{\mu}_P = 1$.

$\tilde{\omega}_S$	$\tilde{\omega}_P$	$M_{\max}$	$M_{\min}$
0.7109	0.8144–0.8261	0.785	0.671
0.719	0.8144–0.839	0.85	0.612
0.722	0.8152–0.8427	0.867	0.598
0.73	0.8178–0.852	0.904	0.57

[1] Marco Raveri, Wayne Hu, Timothy Hoffman, and Lian-Tao Wang, Partially acoustic dark matter cosmology and cosmological constraints, Phys. Rev. D **96**, 103501 (2017).

[2] Mark Hindmarsh and Owe Philipsen, Dark matter of weakly interacting massive particles and the QCD equation of state, Phys. Rev. D **71**, 087302 (2005).

[3] Bernard Carr and Florian Kühnel, Primordial black holes as dark matter: Recent developments, Annu. Rev. Nucl. Part. Sci. **70**, 355 (2020).

[4] Joshua Eby, Chris Kouvaris, Niklas Grønlund Nielsen, and L. C. R. Wijewardhana, Boson stars from self-interacting dark matter, J. High Energy Phys. 02 (2016) 028.

[5] Jiajun Chen, Xiaolong Du, Erik W. Lentz, David J. E. Marsh, and Jens C. Niemeyer, New insights into the formation and growth of boson stars in dark matter halos, Phys. Rev. D **104**, 083022 (2021).

[6] R. Sharma, S. Karmakar, and S. Mukherjee, Boson star and dark matter, arXiv:0812.3470.

[7] Fintan D. Ryan, Spinning boson stars with large self-interaction, Phys. Rev. D **55**, 6081 (1997).
[8] Joao Luis Rosa, Caio F. B. Macedo, and Diego Rubiera-Garcia, Imaging compact boson stars with hot-spots and thin accretion disks, Phys. Rev. D **108**, 044021 (2023).
[9] Diego F. Torres, S. Capozziello, and G. Lambiase, Supermassive boson star at the Galactic center?, Phys. Rev. D **62**, 104012 (2000).
[10] R. A. Swaters, B. F. Madore, and M. Trewhella, High-resolution rotation curves of low surface brightness galaxies, Astrophys. J. **531**, L107 (2000).
[11] Lucio Mayer and James Wadsley, The formation and evolution of bars in low surface brightness galaxies with cold dark matter haloes, Mon. Not. R. Astron. Soc. **347**, 277 (2004).
[12] Alexandre M. Pombo and Ippocratis D. Saltas, A Sun-like star orbiting a boson star, Mon. Not. Roy. Astron. Soc. **524**, 4083 (2023).
[13] J. L. Rosa, P. Garcia, F. H. Vincent, and V. Cardoso, Observational signatures of hot spots orbiting horizonless objects, Phys. Rev. D **106**, 044031 (2022).
[14] Lorenzo Annulli, Vitor Cardoso, and Rodrigo Vicente, The response of ultralight dark matter to supermassive black holes and binaries, Phys. Rev. D **102**, 063022 (2020).
[15] David J. Kaup, Klein-Gordon Geon, Phys. Rev. **172**, 1331 (1968).
[16] Remo Ruffini and Silvano Bonazzola, Systems of self-gravitating particles in general relativity and the concept of an equation of state, Phys. Rev. **187**, 1767 (1969).
[17] Hong-Bo Li, Yan-Bo Zeng, Yan Song, and Yong-Qiang Wang, Self-interacting multistate boson stars, J. High Energy Phys. 04 (2021) 042.
[18] Felix Kling and Arvind Rajaraman, Profiles of boson stars with self-interactions, Phys. Rev. D **97**, 063012 (2018).
[19] Franz E. Schunck and Diego F. Torres, Boson stars with generic self-interactions, Int. J. Mod. Phys. D **09**, 601 (2000).
[20] Nicolas Sanchis-Gual, Carlos Herdeiro, and Eugen Radu, Self-interactions can stabilize excited boson stars, Classical Quantum Gravity **39**, 064001 (2022).
[21] Ph. Jetzer, Stability of charged boson stars, Phys. Lett. B **231**, 433 (1989).
[22] P. Jetzer, P. Liljenberg, and B.-S. Skagerstam, Charged boson stars and vacuum instabilities, Astropart. Phys. **1**, 429 (1993).
[23] Ph. Jetzer and J. J. Van Der Bij, Charged boson stars, Phys. Lett. B **227**, 341 (1989).
[24] Federico García and Ignacio Salazar Landea, Charged Proca stars, Phys. Rev. D **94**, 104006 (2016).
[25] S. Kumar, U. Kulshreshtha, and D. Shankar Kulshreshtha, Boson stars in a theory of complex scalar fields coupled to the $U(1)$ gauge field and gravity, Classical Quantum Gravity **31**, 167001 (2014).
[26] R. Harrison, I. Moroz, and K. P. Tod, A numerical study of the Schrodinger-Newton equation 2: The time-dependent problem, arXiv:math-ph/0208046.
[27] Vanda Silveira and Claudio M. G. de Sousa, Boson star rotation: A Newtonian approximation, Phys. Rev. D **52**, 5724 (1995).
[28] Hong-Bo Li, Shuo Sun, Tong-Tong Hu, Yan Song, and Yong-Qiang Wang, Rotating multistate boson stars, Phys. Rev. D **101**, 044017 (2020).
[29] Shijun Yoshida and Yoshiharu Eriguchi, Rotating boson stars in general relativity, Phys. Rev. D **56**, 762 (1997).
[30] Burkhard Kleihaus, Jutta Kunz, and Meike List, Rotating boson stars and Q-balls, Phys. Rev. D **72**, 064002 (2005).
[31] Nils Siemonsen and William E. East, Stability of rotating scalar boson stars with nonlinear interactions, Phys. Rev. D **103**, 044022 (2021).
[32] Richard Brito, Vitor Cardoso, Carlos A. R. Herdeiro, and Eugen Radu, Proca stars: Gravitating Bose-Einstein condensates of massive spin 1 particles, Phys. Lett. B **752**, 291 (2016).
[33] Felix Finster, Joel Smoller, and Shing-Tung Yau, Particle-like solutions of the Einstein-Dirac equations, Phys. Rev. D **59**, 104020 (1999).
[34] Davide Guerra, Caio F. B. Macedo, and Paolo Pani, Axion boson stars, J. Cosmol. Astropart. Phys. 09 (2019) 061; 06 (2019) E01.
[35] Yan-Bo Zeng, Hong-Bo Li, Shi-Xian Sun, Si-Yuan Cui, and Yong-Qiang Wang, Rotating hybrid axion-miniboson stars, arXiv:2103.10717.
[36] Jorge F. M. Delgado, Carlos A. R. Herdeiro, and Eugen Radu, Rotating axion boson stars, J. Cosmol. Astropart. Phys. 06 (2020) 037.
[37] P. V. P. Cunha, J. Grover, C. Herdeiro, E. Radu, H. Runarsson, and A. Wittig, Chaotic lensing around boson stars and Kerr black holes with scalar hair, Phys. Rev. D **94**, 104023 (2016).
[38] M. Grould, Z. Meliani, F. H. Vincent, P. Grandclément, and E. Gourgoulhon, Comparing timelike geodesics around a Kerr black hole and a boson star, Classical Quantum Gravity **34**, 215007 (2017).
[39] J. L. Rosa and D. Rubiera-Garcia, Shadows of boson and Proca stars with thin accretion disks, Phys. Rev. D **106**, 084004 (2022).
[40] Djuna Croon, JiJi Fan, and Chen Sun, Boson star from repulsive light scalars and gravitational waves, J. Cosmol. Astropart. Phys. 04 (2019) 008.
[41] Tim Dietrich, Serguei Ossokine, and Katy Clough, Full 3D numerical relativity simulations of neutron star–boson star collisions with BAM, Classical Quantum Gravity **36**, 025002 (2019).
[42] Miguel Bezares and Carlos Palenzuela, Gravitational waves from dark boson star binary mergers, Classical Quantum Gravity **35**, 234002 (2018).
[43] Juan Calderon Bustillo, Nicolas Sanchis-Gual, Samson H. W. Leong, Koustav Chandra, Alejandro Torres-Forne, Jose A. Font, Carlos Herdeiro, Eugen Radu, Isaac C. F. Wong, and T. G. F. Li, Searching for vector boson star mergers within LIGO-Virgo intermediate-mass black-hole merger candidates, arXiv:2206.02551.
[44] Argelia Bernal, Juan Barranco, Daniela Alic, and Carlos Palenzuela, Multi-state boson stars, Phys. Rev. D **81**, 044031 (2010).
[45] M. Alcubierre, J. Barranco, A. Bernal, J. C. Degollado, A. Diez-Tejedor, M. Megevand, D. Nunez, and O. Sarbach, ℓ-boson stars, Classical Quantum Gravity **35**, 19LT01 (2018).

[46] M. Alcubierre, J. Barranco, A. Bernal, J. C. Degollado, A. Diez-Tejedor, M. Megevand, D. Núñez, and O. Sarbach, Dynamical evolutions of ℓ-boson stars in spherical symmetry, Classical Quantum Gravity **36**, 215013 (2019).

[47] F. H. Vincent, Z. Meliani, P. Grandclément, E. Gourgoulhon, and O. Straub, Imaging a boson star at the Galactic center, Classical Quantum Gravity **33**, 105015 (2016).

[48] C. A. R. Herdeiro, A. M. Pombo, E. Radu, P. V. P. Cunha, and N. Sanchis-Gual, The imitation game: Proca stars that can mimic the Schwarzschild shadow, J. Cosmol. Astropart. Phys. 04 (2021) 051.

[49] A. M. Pombo, J. M. S. Oliveira, and N. M. Santos, Coupled scalar-Proca soliton stars, Phys. Rev. D **108**, 044044 (2023).

[50] Chen Liang, Ji-Rong Ren, Shi-Xian Sun, and Yong-Qiang Wang, Dirac-boson stars, J. High Energy Phys. 02 (2023) 249.

[51] C. A. R. Herdeiro, A. M. Pombo, and E. Radu, Asymptotically flat scalar, Dirac and Proca stars: Discrete vs. continuous families of solutions, Phys. Lett. B **773**, 654 (2017).

[52] C. A. R. Herdeiro, J. M. S. Oliveira, A. M. Pombo, and E. Radu, Virial identities in relativistic gravity: 1D effective actions and the role of boundary terms, Phys. Rev. D **104**, 104051 (2021).

[53] C. A. R. Herdeiro, J. M. S. Oliveira, A. M. Pombo, and E. Radu, Deconstructing scaling virial identities in general relativity: Spherical symmetry and beyond, Phys. Rev. D **106**, 024054 (2022).